Hydrogen on In2O3 : Reducibility, Bonding, Defect Formation, and Reactivity

ARTICLE *in* THE JOURNAL OF PHYSICAL CHEMISTRY C · APRIL 2010

Impact Factor: 4.77 · DOI: 10.1021/jp1017423

Hydrogen on In_2O_3: Reducibility, Bonding, Defect Formation, and Reactivity

Thomas Bielz,[†] Harald Lorenz,[†] Wilfrid Jochum,[‡,†] Reinhard Kaindl,[§] Frederik Klauser,[†] Bernhard Klötzer,[†] and Simon Penner*[,†]

Institute of Physical Chemistry, University of Innsbruck, Innrain 52a, A-6020 Innsbruck, Austria, and Institute of Mineralogy and Petrography, University of Innsbruck, Innrain 52d, A-6020 Innsbruck, Austria

Received: February 26, 2010; Revised Manuscript Received: April 14, 2010

The adsorption, bonding, defect formation, and reactivity of hydrogen on different In_2O_3 powder samples were studied by a combination of volumetric adsorption, thermal desorption, diffraction, and spectroscopic techniques. Surface reduction was observed in dry hydrogen up to 400 K, followed by reduction of surface-near regions. Above 500 K bulk reduction, along with the formation of metallic In, sets in. Raman spectra indicate a considerable reordering of the In_2O_3 structure in this temperature regime. Despite their TPD proven presence, the related adsorbed H-containing species were not detectable by Fourier transform infrared spectroscopy and/or Raman spectroscopy, in strong contrast to related experiments on β-Ga_2O_3. Hydrogen-induced oxygen vacancies were found to be easily replenished by traces of water in the gas feed.

1. Introduction

Due to its exceptional physicochemical properties, In_2O_3 has attracted increased interest in a variety of research fields, including sensor technology,[1−3] heterogeneous catalysis,[4−6] or as an application in electronic devices.[7] Since In_2O_3 is an n-type semiconductor, it is renowned for its sensitivity toward both oxidizing (e.g., NO_2 or SO_2) and reducing (e.g., H_2 or CO) gases.[3] Recently, the importance of these special properties in catalytic studies, especially steam reforming reactions, has been highlighted.[4,5] In the case of methanol steam reforming, this results in an almost 100% CO_2 selectivity.[5] However, the basic principles of catalytic activity and selectivity are not yet understood in full detail. This especially concerns the interaction of the steam reforming reactants with different In_2O_3 surfaces and structures. Of highest importance in this respect is the easy reducibility of In_2O_3, leading to mixtures of In_2O_3 and In metal for excessive reduction in hydrogen at temperatures $T \geq 673$ K.[8] The influence of various gas atmospheres (oxygen, carbon monoxide, water) on valence band photoemission spectra and surface conductivity has also been highlighted.[9] Since water is the most important steam reforming reactant, its interaction with In_2O_3 is of particular importance, especially on reduced In_2O_3 surfaces, as the reoxidation of the surface by water should produce hydrogen. Studies on the decomposition of water on the CO- and H_2-reduced In_2O_3 surfaces revealed an easy removal of surface oxygen by reduction in H_2 or CO at 673 K, but only an insufficient oxygen replenishment upon reoxidation with water, which was tentatively explained by the formation of In metal during the reduction process.[6] This behavior, however, already indicates facile water activation on reduced In_2O_3 surfaces, which is a key process in determining the CO_2 selectivity of methanol steam reforming over In_2O_3.

On the basis of these previous results, the present contribution aims at a better understanding of the reduction processes of In_2O_3 by hydrogen, especially at lower reduction temperatures, where the formation of In metal is suppressed. The influence of different surface chemistries and surface defect concentrations on the adsorption of hydrogen and water will be discussed. Particular emphasis will be given to a correlation to the previously studied CO_2-unselective Ga_2O_3 sample[10] in methanol steam reforming, with the ultimate goal to reveal the selectivity difference of both oxides in methanol steam reforming. This task was accomplished by using volumetric adsorption measurements to quantify the adsorbed molecules, thermal desorption spectroscopy to study the different adsorption sites on differently pretreated In_2O_3 surfaces, electric impedance measurements to reveal the influence of reduction on conductivity, FT-infrared spectroscopy to reveal the nature of adsorbed species, and X-ray diffraction (XRD) and Raman spectroscopy to study structural transformations during reduction and adsorption. To eventually discriminate surface and bulk reduction, three different types of In_2O_3 with different surface areas will be examined.

2. Experimental Section

2.1. Materials. Three different In_2O_3 samples were used in this work. The samples comprise a commercial In_2O_3 sample (Alfa Aesar 99.999%, surface of 1 m^2/g as determined by nitrogen adsorption at 77 K according to BET) and two high surface area samples prepared by thermal decomposition of indium hydroxide by stepwise heating in air to a final temperature of 973 K. To prepare the $In(OH)_3$ samples, a solution of indium nitrate was first obtained by dissolution of metallic In (Goodfellow, 99.999%) in dilute nitric acid. Subsequently, indium hydroxide was prepared either by precipitation from this solution by adding aqueous ammonia directly or by precipitation after performing an additional oxidation step by adding a stoichiometric excess of 30% H_2O_2. The resulting precipitates were filtrated and dried in air at 423 K, yielding colorless crystalline powders, which then were subjected to decomposition toward In_2O_3, as described above. This procedure yielded two high surface area pure In_2O_3 samples of 19 and 15 m^2/g as proven by BET and XRD. For both higher surface area samples a reflex broadening due to their smaller particle sizes was observed, but still only crystalline bcc In_2O_3 reflections were

* To whom correspondence should be addressed. E-mail: simon.penner@uibk.ac.at. Phone: 00435125075056. Fax: 00435125072925.
[†] Institute of Physical Chemistry, University of Innsbruck.
[‡] Present address: ADLER-Werk Lackfabrik, Johann Berghofer GmbH & Co KG, Bergwerkstrasse 22, A-6130 Schwaz, Austria.
[§] Institute of Mineralogy and Petrography, University of Innsbruck.

10.1021/jp1017423
Published on Web 04/26/2010

present (not shown). The related Raman spectroscopy experiments for both samples, however, showed remarkable differences: apparently, dissolution of In metal in dilute nitric acid did not yield 100% oxidation of In^0 to In^{3+}. As a consequence, a more defective 19 m^2/g sample containing traces of reduced In species (presumably In^+) was generated, giving rise to extra Raman modes as discussed in section 3.5.

Hydrogen, helium, and oxygen were supplied by Messer-Griesheim as high-purity gases. Hydrogen was further purified by passing through an oxygen-removing purifier. Condensable contaminants were removed from helium and hydrogen by liquid nitrogen traps. For oxygen a trap cooled with liquid nitrogen/ethanol was used.

2.2. Volumetric Apparatus. The volumetric measurements were performed in an all-glass apparatus[10] equipped with metal bellow valves (Witeg), a Baratron pressure transducer (MKS), and mass flow controllers (MKS). To enable volumetric measurements up to 1000 K, the reactor part containing the sample was made of quartz. The samples were treated for 1 h in 1 bar of flowing dry hydrogen at a typical flow rate of 60 mL/min at different temperatures (373−573 K). After that the sample was evacuated at room temperature down to a base pressure of about 5×10^{-7} mbar and heated in high vacuum to 923 K at a rate of 10 deg/min (TPD measurements), followed by cooling under vacuum to 313 K. The temperature-programmed oxidation (TPO) measurements allowed us to study the reoxidation process and the amount of oxygen required for complete reoxidation and quenching of lattice defects.

2.3. Conductivity Apparatus. The impedance cell (described in ref 10) is suited for gas treatments compatible with those in the volumetric measurements. Heating was provided by a tubular oven and controlled by a thermocouple situated in the reactor about 5 mm downstream of the sample and a Micromega PID temperature controller. The sample impedance was measured by an IM6e impedance spectrometer (Zahner-Elektrik), which supplied data on the impedance and the phase angle of the current as a function of voltage (20 mV) in a frequency range of 0.1 to 1 MHz. For all In_2O_3 measurements described herein, a very low excitation frequency of 1 Hz and a stimulation voltage of 20 mV using two circular gold electrodes forming a plate capacitor and exerting a pressure of 1 bar in a vertical quartz tube was used.[10] For a variety of differently reduced In_2O_3 samples only ohmic resistivity could be verified upon variation of the excitation frequency.

2.4. Raman Spectroscopy. Confocal Raman spectra were obtained with a Horiba Jobin Yvon LabRam-HR 800 Raman miro-spectrometer. The samples were excited by the 532 nm emission line of a 100 mW Nd:YAG and the 633 nm emission line of a 17 mW He−Ne laser. Size and power of the laser spot on the surface was approximately 1 μm and 1 mW, respectively. A grating with 1800 lines/mm was used. The spectral resolution, determined by measuring the Raleigh line, ranged from 1.4 to 2 cm^{-1}. The dispersed light was collected by a 1024 × 256 open electrode CCD detector. Confocal pinhole and spectrometer entrance slit were set to 1000 and 100 μm, respectively. Spectra were recorded unpolarized. The accuracy of Raman line shifts on the order of 0.5 cm^{-1} was achieved by adjusting the zero-order position of the grating and regularly checked by measuring the Rayleigh line.

2.5. FT-IR. FTIR spectra were recorded in transmission mode on a Perkin-Elmer 2000 FTIR spectrometer. After a series of unsuccessful attempts to prepare both sufficiently stable and transparent IR specimens by In_2O_3 powder pressing, the most successful routine turned out to be the decomposition of an indium nitrate pellet (prepared from ∼60 mg of anhydrous indium nitrate powder) by stepwise heating to 973 K in air. The main advantage of this procedure is, except for the high stability of the pellets, an extremely low level of OH-related intensity. The so-treated pellet was transferred quickly into the IR cell, which is equipped with a ring-shaped furnace, allowing for in situ treatments in different gas atmospheres up to 773 K. The initial IR spectrum after transfer showed almost no OH vibrations or features due to undecomposed indium nitrate and hence served as a good starting point for adsorption and H_2 reduction experiments. Reduction was carried out in streaming hydrogen (purified with a liquid nitrogen trap) at a heating rate of 5 deg/min to the required temperatures (maximum temperature: 473 K) and the spectrum was taken directly at the respective temperature, without a further cooling step.

2.6. X-ray Diffraction. X-ray diffraction experiments were performed ex-situ under ambient conditions with a Siemens D5000 spectrometer and Cu Kα radiation (1.54178 Å) at 300 K.

3. Results and Discussion

3.1. Volumetric Adsorption of H_2. Before each TPR experiment, the samples were fully oxidized by heating in 1 bar of dry flowing O_2 to 973 K. After heating at 973 K for 1 h, the samples were cooled to room temperature in flowing dry O_2 followed by pumping down the TPR cell to about 5×10^{-7} mbar. Subsequently, 93 mbar of dry hydrogen was admitted at 313 K. The volumetric experiments involved heating from 313 K to the final temperature of 673 K at a linear rate of 10 deg/min, maintaining the maximum temperature for 10 min, and then cooling to 313 K at a rate of 10 deg/min.

Figure 1 illustrates the hydrogen uptake as a function of temperature. It can be concluded that during the heating ramp the uptake of hydrogen is strongly influenced by kinetic limitations, especially from the fact that the full hydrogen uptake obtained at the highest temperature remains constant or even increases upon cooling for both samples. For the small surface area sample (1 m^2/g), the uptake kinetics during heating leads to at least two discernible steps of hydrogen uptake, which must be related to kinetically different ways to bind hydrogen on In_2O_3. On the high-surface area sample, saturation of hydrogen uptake is already reached around 500 K and the last step (above 520 K) observed on the 1 m^2/g sample is absent. Saturation for the 1 m^2/g sample is not even obtained at $T > 600$ K (plateau 600−673 K), which can be clearly inferred from the isothermal increase of hydrogen uptake at 673 K from 9.6 to 10.4 μmol/m^2 within 10 min. Obviously even at 673 K kinetic limitations for the high-temperature hydrogen uptake process on the 1 m^2/g sample sustain. The uptake curves for both samples coincide up to ∼390 K, which can be addressed to predominant surface reduction of both samples irrespective of the total sample amount. This result is further corroborated by temperature-programmed reoxidation (cf. Figure 3), showing a coincidence of the number of vacancy sites per m^2 up to about 420 K prereduction temperature. Furthermore, impedance measurements (cf. Figure 8) reveal a transition to almost metallic conductivity at already 400 K upon reduction in flowing dry hydrogen. In the temperature regime 400−500 K, the number of vacancies increases, i.e. the reduction degree increases by approximately a factor of 2−3, eventually resulting in some form of surface reconstruction or reordering. A clear hint for such a process is inferred by the corresponding Raman spectra on all studied powder samples reduced at 523 K and above (cf section 3.5), which show additional features due to a structural reordering starting from the In_2O_3 bcc lattice. In any case, this

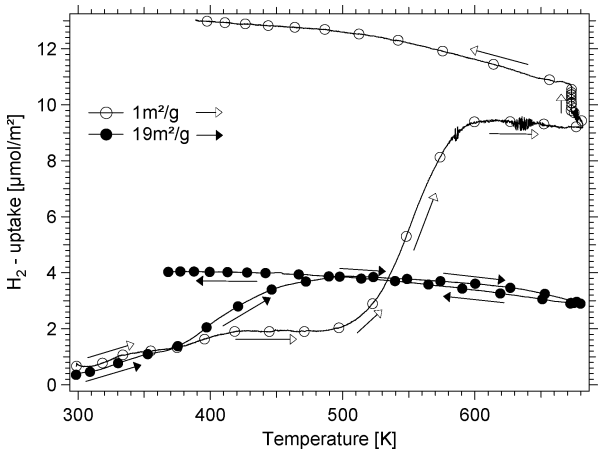

Figure 1. Volumetric adsorption measurement of hydrogen consumption during a temperature-programmed reduction (TPR) heating and cooling cycle between 313 and 673 K. The samples were exposed to 93 mbar initial H_2 pressure at 313 K before the ramp was started. Linear heating and cooling rate: 10 deg/min.

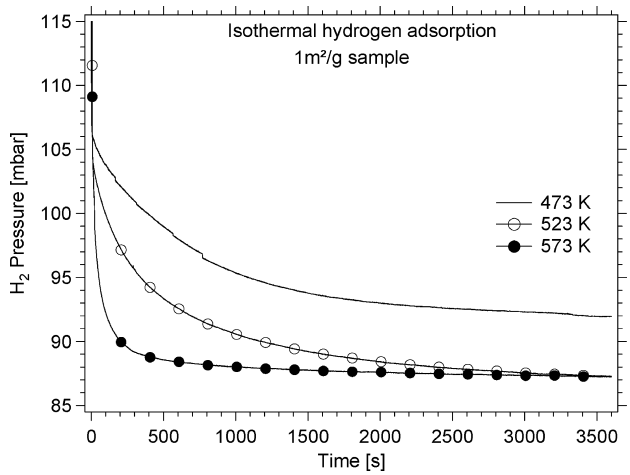

Figure 2. Isothermal volumetric hydrogen adsorption at 473, 523, and 573 K on the 1 m^2/g In_2O_3 sample. The sample was exposed to about 115 mbar of H_2 before the uptake was monitored for 60 min at each temperature.

must include the formation of In centers with oxidation states <+3. Above 500 K, additional bulk-related reduction takes place, which is clearly corroborated by XRD measurements (cf. Figure 6), showing formation of metallic In at least after reduction at 573 K, and by the kinetics of hydrogen uptake.

To discriminate the different kinetic regimes of hydrogen uptake on the 1 m^2/g sample in Figure 1, isothermal kinetic experiments on this sample were additionally performed. On the one hand, the kinetics of isothermal volumetric hydrogen uptake was measured at constant temperatures of 473, 523, and 573 K (Figure 2). On the other hand, as will be described in section 3.4 (cf. Figure 5), the population of the different TPD states was also isothermally studied as a function of exposure time. The results of the isothermal volumetric hydrogen uptake are consistent with the interpretation of Figure 1 in terms of at least two discernible kinetic regimes of hydrogen population. At 573 K (cf. Figure 1, upper end of stepwise increase of hydrogen uptake), the isothermal hydrogen uptake directly approaches the final value of ~9 μmol/m^2 (see Figure 1) after only 400 s. Thereafter, a rather slow uptake of hydrogen up to 3600 s may be associated with the even slower process discussed in the context of Figure 1 as isothermal uptake at 673 K. In

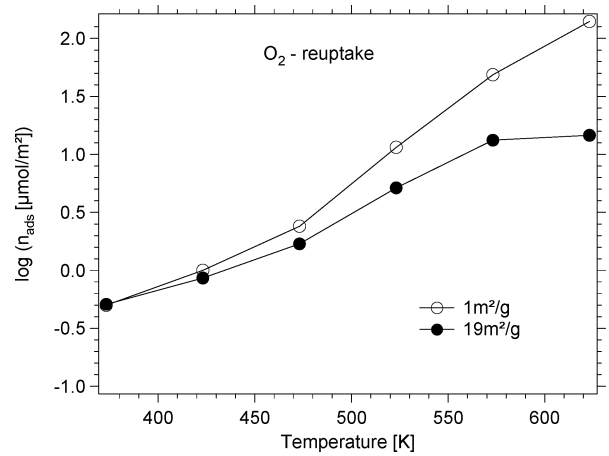

Figure 3. Whole O_2-reuptake following reduction in dry hydrogen and H_2-TPD on the 1 and 19 m^2/g In_2O_3 sample.

contrast, at 523 K (cf. Figure 1, lower end of stepwise increase of hydrogen uptake), the reduction process associated with this step is strongly delayed. In fact, it takes 3600 s to approach the same degree of reduction as observed at 573 K. At 473 K (cf. Figure 1, first plateau region), the reduction process associated with the 523−573 K step of Figure 1 is kinetically not accessible on the time scale of 1 h. Thus, the final degree of reduction after 1 h stagnates at the 423−500 K plateau level of Figure 1.

If the same total surface area is provided experimentally (2.1685 g of 1 m^2/g sample vs 0.1141 g of 19 m^2/g sample), the main difference between the low and high surface area sample clearly is the increased availability of "deep bulk" binding sites for hydrogen in the 1 m^2/g sample. Assuming that for the 19 m^2/g sample a true equilibrium saturation of both surface and bulk-related hydrogen uptake (~3 μmol/m^2 corresponding to ~57 μmol/g) was reached at 673 K, the corresponding value for the 1 m^2/g sample could consequently amount to 19 times higher values, i.e., around 57 μmol/m^2. However, from the combined information of still persisting kinetic limits of hydrogen uptake on the 1 m^2/g sample at 673 K and only ~10 μmol/m^2 hydrogen uptake at maximum, we conclude that deeper bulk migration and storage of hydrogen is much slower for this sample even at the highest temperatures. Whether this effect can be solely attributed to the larger particle diameters, and thus to a more demanding accessibility of deeper bulk sites, or also to major differences in structural defectivity (e.g., an increased amount of grain boundaries facilitating transport processes), cannot be distinguished on the basis of our experiments.

3.2. Temperature-Programmed Reoxidation (TPO) of Reduced In_2O_3. As an alternative route for studying defect formation in dry H_2, the O_2 uptake after In_2O_3 reduction at different temperatures was measured (Figure 3; oxidation was carried out in 1 bar of dry O_2 at 973 K for 1 h). It is worth noting that the O_2 reuptake was determined *after* performing the corresponding hydrogen TPD experiments, that is, only the empty lattice vacancies, but no defect-related H species, are quenched by titration with O_2. An total of ~0.5 μmol/m^2 vacancies were already detectable on both samples after reduction at 373 K and subsequent thermal desorption. O_2 uptake was almost equal for both samples (2.1685 g of 1 m^2/g sample vs 0.1141 g of 19 m^2/g sample, i.e. 2.1685 m^2) up to the 423 K prereduction temperature, as shown in Figure 3. Again, this behavior can be attributed to the predominant quenching of surface-related vacancies. Above 423 K, a clear difference between both samples was evolving. The sample with more

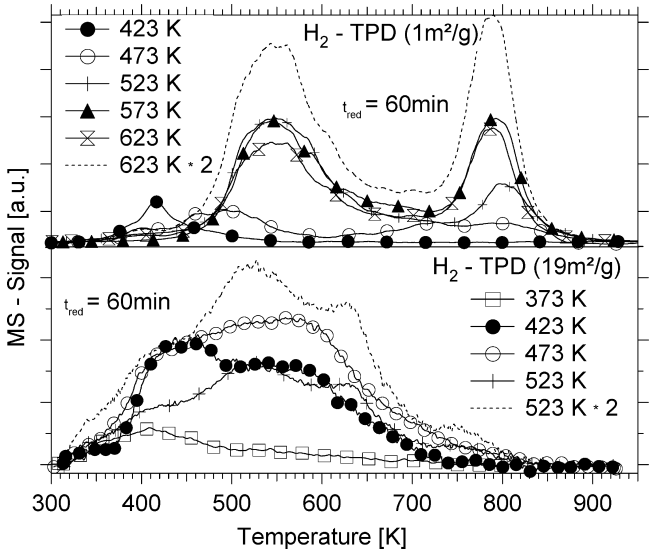

Figure 4. Temperature-programmed H_2 desorption spectra as a function of the reduction temperature for the 1 (upper panel) and 19 m^2/g sample (lower panel). A linear heating and cooling rate of 10 deg/min was applied. Isothermal reduction at each temperature was carried out for 60 min each. All segments of the ramp were performed in a 60 mL/min flow of 1 bar of LN_2-dried H_2.

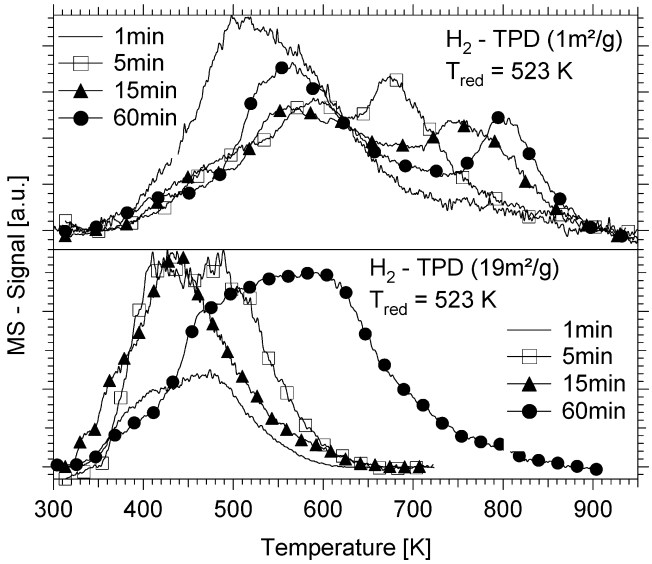

Figure 5. Temperature-programmed H_2 desorption spectra as a function of reduction time at 523 K for the 1 (upper panel) and 19 m^2/g sample (lower panel). Linear heating rate 10 deg/min.

extended bulk clearly shows a larger relative contribution of surface-near and bulk-related vacancies, as jointly deduced from Figures 1 and 3.

3.3. Temperature-Programmed Desorption (TPD). The effect of the hydrogen reduction temperature and time on the formation of specific hydrogen binding states and oxygen vacancies was further studied by TPD. Figure 4 shows the temperature-dependent TPD spectra of the two In_2O_3 samples (1 m^2/g, upper panel; 19 m^2/g, lower panel). The hydrogen reduction/adsorption cycle involved heating from room temperature to different reduction temperatures (373, 423, 473, 523, 573 K) at a rate of 10 deg/min in a constant flow of 60 mL/min of dry H_2 (1 bar), maintaining the sample in the H_2 flow at the final reduction temperature for 1 h, and then cooling to room temperature again at a rate of 10 deg/min. Before the TPD spectra were obtained, the sample was evacuated at room

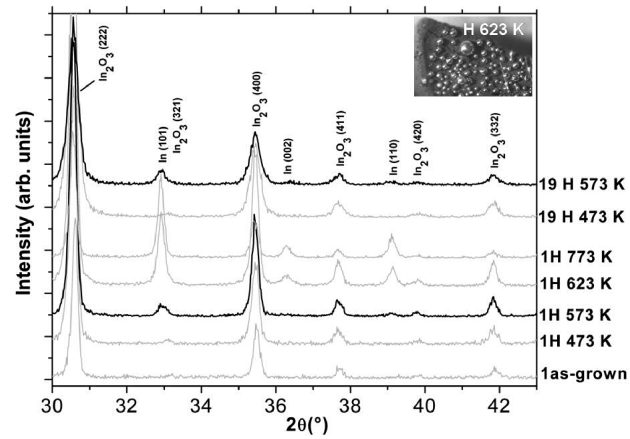

Figure 6. XRD spectra of the 1 and 19 m^2/g In_2O_3 sample after different treatments in 1 bar of dry H_2. The inset shows a photograph of the In_2O_3 pellet after reduction of the 1 m^2/g sample at 623 K for 60 min in 1 bar of dry H_2.

temperature for about 20 min at $\sim 5 \times 10^{-7}$ mbar. As a consequence of the different kinetic regimes of H_2 uptake (cf. Figure 1) we also observed the population of different adsorption states of hydrogen on the 1 m^2/g sample, as shown in Figure 4. The first desorption state, with a maximum at ~410 K, is thus assigned to the reversal of purely surface-limited hydrogen bonding. The second rate maximum at ~550 K is consequently assigned to desorption from surface-near binding sites. And finally, the high-temperature maximum at ~790 K is tentatively related to bulk-migration of hydrogen, and starts to dominate at reduction temperatures of $T > 523$ K. The population of more and more strongly bound hydrogen with increasing reduction temperature, herein also observed for In_2O_3, is a frequently observed kinetic phenomenon[10] and can be associated with a higher activation barrier for the generation of increasingly higher coordinated binding sites (a process that is finally associated with structural changes as shown in the Raman spectra of section 3.5), and/or with increasing transport limitations, e.g., in and out of the deeper bulk region. For the high surface area sample, the high-temperature peak at ~790 K is entirely missing at even the highest reduction temperatures. An effect, equally observed on both samples, albeit at slightly different temperatures, is related to the loss of TPD area at reduction temperatures $T \geq$ 573 K for the 1 m^2/g and $T \geq$ 523 K for the 19 m^2/g sample. As will be shown in detail in Figure 6, this loss of active hydrogen binding sites is associated with formation of metallic In, being incapable of hydrogen adsorption. This effect is demonstrated for both samples at 623 (1 m^2/g) and 523 K (19 m^2/g) by multiplying the intensity by a factor of ~2 (dotted lines), revealing its possible shape, without the loss of oxide-related binding sites due to In metal formation. From the XRD measurements it also appears that In metal formation is somewhat easier on the 19 m^2/g sample exhibiting smaller grains, giving rise to faster In metal formation at slightly lower reduction temperatures.

The kinetic limitation of hydrogen uptake that has already been demonstrated in Figures 1 and 2 for the 1 m^2/g sample is also obvious from the temperature series of Figure 4, because at reduction temperatures above 523 K (in the middle of the 520 to 600 K step of Figure 1, 1 m^2/g) complete population of the corresponding high-temperature binding sites (peak at $T \approx$ 800 K) can be achieved within approximately 1 h. A reduction temperature of 473 K is obviously not sufficient to populate this high-temperature binding site (in good agreement with the kinetics shown in Figure 2). Again, we can only hypothesize

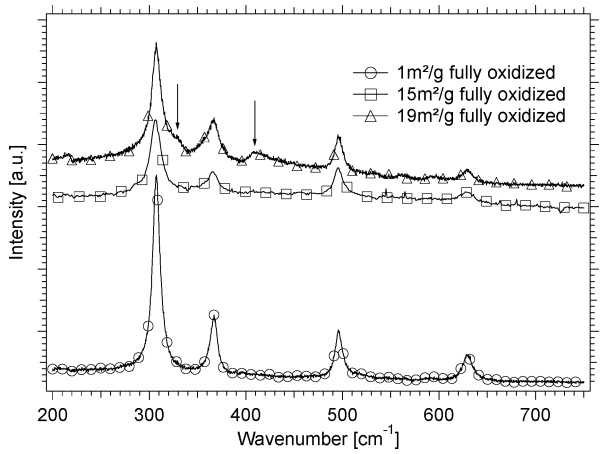

Figure 7. Raman spectra of the fully oxidized 1, 15, and 19 m^2/g In_2O_3 sample.

about the nature of the high-temperature state. In a perfect In_2O_3 lattice, both the formation of oxygen vacancies in deep bulk regions and their population with hydrogen species, but also the reversal of these processes involve demanding transport processes over mesoscopic lattice dimensions. Likely, the barrier for oxide ion mobility in the bcc In_2O_3 lattice has to be overcome to create such defects. Logically, oxide ion diffusion out of followed by hydrogen diffusion into the lattice are essential prerequisites to populate defects in deeper regions. From the experiments dealing with reversible lattice defect formation at different oxygen partial pressures (Figure 11, section 3.6), we deduced that the mobility of lattice oxide ions must be already rather high at temperatures $T \approx 673$ K. The same kinetic limitations appear to apply to the depopulation of hydrogen binding sites in the deeper lattice regions, and thus the corresponding desorption state is shifted to temperatures as high as 800 K. The desorption state at ~550 K, accordingly, does not require oxygen ion mobility for mass transport and is thus assigned to hydrogen binding states in near-surface or some kind of "internal surface" binding sites more easily accessible for hydrogen (e.g., at or close to grain boundaries or structural lattice defects). In the latter case, a direct surface or interface reaction of hydrogen with oxide ions to form water, followed by direct diffusion of water to the gas phase is conceivable. This process is apparently more demanding with respect to diffusion for deep bulk exchange of oxygen by hydrogen, which requires diffusion of O^{2-} out of the lattice over a certain distance to the surface, reaction at the surface with hydrogen to form water, and finally diffusion of hydrogen toward the so-formed lattice vacancies as available binding sites. As mentioned above and shown in the lower panel of Figure 4, the high-temperature peak at ~790 K is strongly underrepresented on the 19 m^2/g sample. Therefore, the high surface area sample exhibits a strongly dominant contribution of the surface-near processes, in addition to the fact that the total number of potential bulk binding sites is much lower, due to the smaller average crystallite size, as confirmed by SEM imaging (not shown) and XRD (Figure 6). Again, the suppression of hydrogen adsorption at $T \geq 523$ K is a strong hint that In metal formation predominantly takes place in close vicinity to the hydrogen binding sites (and leads to their depletion) at comparable temperatures (cf. Figure 6). The 500−600 K adsorption states highlighted in the lower panel of Figure 4 are thus attributed to predominant surface-related adsorption at any tested reduction temperature and are hence similar to the ~550 K TPD feature on the 1 m^2/g sample (upper panel).

The isothermal exposure series obtained in 1 bar of flowing H_2 at 523 K shown in Figure 5 demonstrates the successive population/depopulation of the different binding sites as a function of prereduction time. With increasing exposure times, an increasing substitution of weakly by more strongly bound hydrogen species is observed, further confirming the kinetically dependent population of different states. This effect is much less pronounced for the high surface area sample.

3.4. X-ray Measurements. To substantiate the process of indium metal formation from In_2O_3 above 523 K, as addressed in the previous section, this transformation was also monitored by XRD. Therefore, the 1 and 19 m^2/g powder was subjected to stepwise heating in flowing hydrogen between 300 and 773 K (Figure 6). The room temperature spectrum of the fully oxidized samples is characteristic of the bcc In_2O_3 structure (only the 1 m^2/g sample is shown; the higher surface area sample shows reflex broadening effects attributed to the smaller grain size, but otherwise the spectra exhibit no marked differences). First changes are notable after reduction at 573 K, where already small peaks of In metal appear (denoted by open squares). In metal formation is more pronounced at temperatures $T > 573$ K. After reduction at 573 K for 1 h, a core of dispersed In metal is formed inside the In_2O_3 pellet, which penetrates to the surface after reduction at 623 K and becomes visible as small bubbles of In metal (see the inset in Figure 6).

From the XRD viewpoint, apparently no crystalline detectable phases of intermediate species of In in reduction states somewhere between In^{3+} and In^0 appear to be present. This is consistent with the fact that so far no diffractional evidence of crystalline In−O suboxidic phases is accessible, although spectroscopically confirmed in ref 11 and in this work (section 3.5). Otsuka et al.[8] suspected that a substoichiometric "In_2O_{3-x}", which is formed during the high-temperature reduction of In_2O_3, in fact always is a mixture of heavily distorted In_2O_3 and In metal, and no intermediate oxides such as In_2O or InO, whose existence is controversly discussed, were detected. Concerning In_2O, formation by reduction of In_2O_3 by hydrogen was reported[12] and a crystalline In_2O phase suspected.[13,14] On the contrary, crystalline In_2O was also discussed as a stoichiometric mixture of In_2O_3 and In metal[15] or as an "intermediate interphase" in a mixture of In_2O_3 and In metal.[16] In any case, no XRD pattern of In_2O could be obtained.[17]

For the 19 m^2/g sample, the observations are quite similar, but by comparing the relative intensities of the (200) peak of tetragonal In (at 2.71 Å/33.1°) with the (400) peak of bcc In_2O_3 (at 2.53 Å/35.3°) after reduction at 573 K, it appears that the ratio In(200)/In_2O_3(400) is slightly larger for the 19 m^2/g as compared to the 1 m^2/g sample. This indicates that In metal formation is further advanced on the high surface area sample at comparable reduction temperatures (see also loss of surface area after isothermal reduction at increasing times, Figure 5).

3.5. Raman Measurements. XRD bulk structure characterization was complemented by Raman measurements. Common IR measurements were only of limited use in monitoring the reduction process of In_2O_3, since only a continuous absorbance increase upon increasing reduction temperature was observed (not shown), but no distinct peaks due to directional In−H bonding (as on Ga_2O_3, see ref 10). Our experiments are based on studies of Yin et al.,[18] dealing with the synthesis and Raman properties of $In(OH)_3$ and In_2O_3 micro- and nanostructures. Our spectra, highlighted in Figures 7 and 8, very much coincide with their Raman spectra obtained for different nanoarchitectures. Four different distinct Raman scattering features are observed for the fully oxidized samples (Figure 7; 1, 15, and 19 m^2/g) in

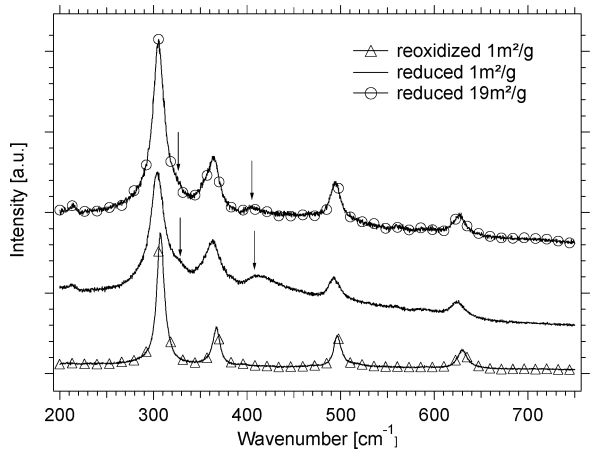

Figure 8. Raman spectra of the reduced 1 and 19 m^2/g In_2O_3 sample (60 min, 523 K, 1 bar of dry H_2) and the reoxidized 1 m^2/g sample.

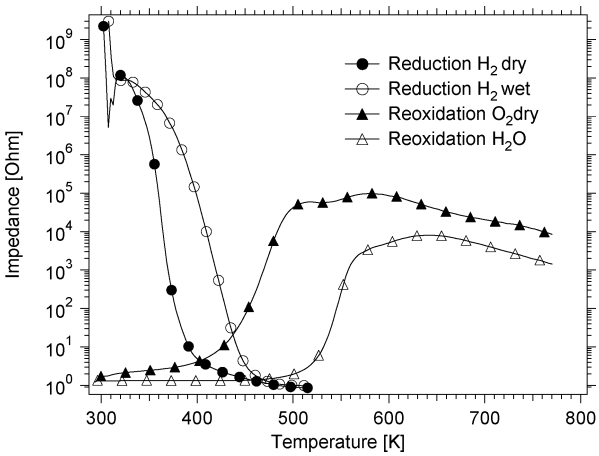

Figure 9. Impedance as a function of temperature after reduction in dry and wet H_2 (6.1 mbar of H_2O in 1 bar of H_2) and after reoxidation in dry O_2 and H_2O (6.1 mbar of H_2O in 1 bar of He).

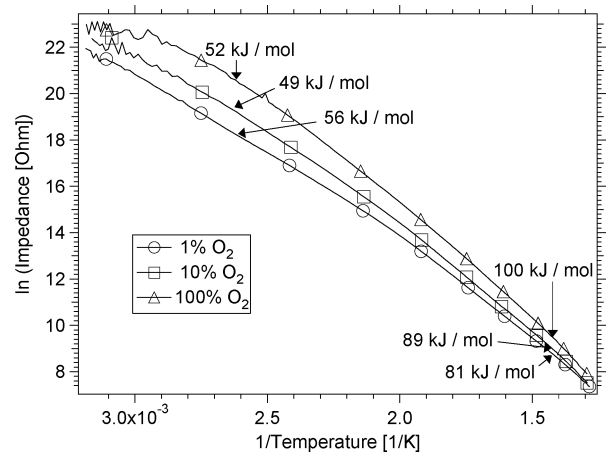

Figure 10. Arrhenius plots ln(impedance) versus inverse temperature at various O_2 partial pressures (100%, 10%, and 1%, corresponding to 1000, 100, and 10 mbar in a O_2/He mixture; total pressure 1000 mbar).

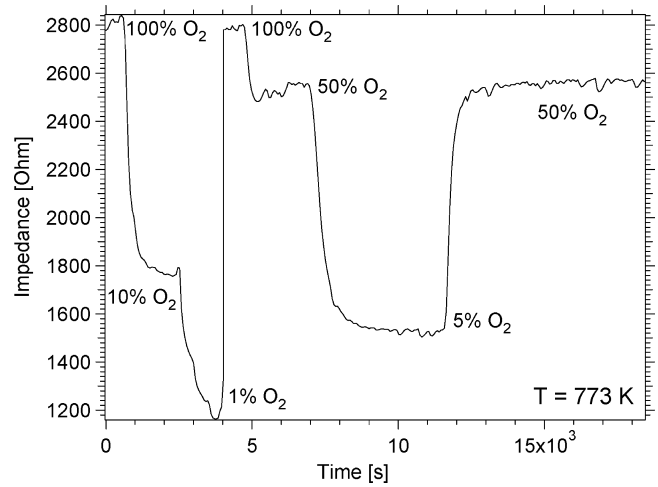

Figure 11. Impedance as a function of the O_2 partial pressure at 773 K. Switching between the various partial pressures indicates that the thermal formation of vacancies is a reversible process.

the spectral range between 200 and 750 cm^1. These are observed at 308, 367, 497, and 630 cm^{-1} and are consistent with Raman-active modes of the bcc In_2O_3 structure. The scattering feature at 308 cm^{-1} is usually interpreted as the bending vibration $\delta(InO_6)$ of octahedrons[19] and the peaks at 497 and 630 cm^{-1} as the stretching vibration $\nu(InO_6)$ of the same unit. The feature at 367 cm^{-1} is assigned to the stretching vibration of the In−O−In unit.[20] The fully oxidized spectra of the 1 and 15 m^2/g samples are almost identical. However, the Raman spectrum of the 19 m^2/g sample exhibits two additional features, that is, a rather well-pronounced shoulder at 330 cm^{-1} and a broad feature at 410 cm^{-1} (marked by arrows). Interestingly, the same features also appear in the Raman spectrum of only the In_2O_3 microbricks shown in Figure 9 of ref 18. In the paper of Yin et al., no detailed explanation on the difference of the Raman spectra of different In_2O_3 morphologies was provided. On the basis of two effects we dare, however, to provide a qualitative explanation for the appearance of these additional features. We first recall that the 15 m^2/g sample was prepared via an additional oxidation step using H_2O_2 in contrast to the 19 m^2/g sample. Second, the Raman spectra taken after reduction of the samples at 573 K (Figure 8) without exception and for all different surface areas show these additional peaks. In contrast, the same peaks were present on the 19 m^2/g sample right from the beginning without any hydrogen reduction (i.e., in the "fully oxidized" state). Despite the absence of distinct XRD features of ordered intermediates, we must address these additional Raman features to the presence of reduced In species, presumably In^+. These species appear to exist near the surface after hydrogen reduction, thus after reoxidation at 673 K, these features disappear again both for the 1 and 15 m^2/g samples, indicating that the surface-near regions of these samples can be reversibly switched between an oxidized and a reduced state. It is also clear that dissolution of In metal in dilute nitric acid (and subsequent precipitation of the hydroxide without H_2O_2 postoxidation) yields only a mixture of In^+ and In^{3+} species, which can only be fully converted to In^{3+} by this additional oxidation step prior to precipitation. Once In^+ species are trapped inside the deeper bulk regions of the indium oxide crystallites, even oxidation in 1 bar of O_2 up to 773 K is not sufficient to remove the related Raman features.

3.6. Electric Impedance Spectroscopy Results. An effective way to monitor the reduction of In_2O_3 to the metallic state is provided by electric impedance spectroscopy. Impedance spectra were collected for all samples discussed in the Experimental Section, but no marked differences were observed. Thus, the measurements presented in this section were performed on the representative 15 m^2/g sample. Reduction and subsequent reoxidation was carried out in dry and wet hydrogen and dry

oxygen and water vapor, respectively (Figure 9). Reduction in dry hydrogen without the presence of water leads to the rapid formation of oxygen vacancies already at low temperatures between 300 and 400 K and finally results in almost metallic conductivity at around 400 K. It is worth remembering that this drop in impedance very much coincides with the hydrogen uptake curves and the corresponding hydrogen adsorption monitored by the TPD spectra (see Figures 1 and 4, respectively; low-temperature uptake region 300−450 K). The presence of a defined water partial pressure (6.1 mbar) leads to in situ quenching of already formed surface oxygen vacancies and shifts the same reduction degree (compared to dry hydrogen) to higher temperatures, that is, to around 470 K. Reoxidation in dry oxygen of a sample formerly reduced in dry hydrogen is kinetically faster at low temperatures as compared to reoxidation with water vapor (400−500 K for oxygen, 520−570 K for water). Note that the trace upon reoxidation at 773 K in dry O_2 approaches a lower impedance value as compared to the fully oxidized state at room temperature, because of the thermal excitation of charge carriers even in dry O_2 at this temperature.

The process of reoxidation and defect quenching with water also has considerable catalytic implications in reforming processes, since hydrogen production from water at reductively generated defects therefore can only occur at a sufficiently fast rate at temperatures $T > 520$ K. Furthermore, when recalling that highly CO_2-selective methanol steam reforming over In_2O_3 starts at around 550 K and accelerates at around 573 K, it is clear that water activation basically proceeds over clean In_2O_3 at temperatures $T > 550$ K.[5]

To gain more insight into the reversibility of vacancy formation and the associated processes, vacancy formation at different oxygen partial pressures was investigated, at temperatures high enough to attain equilibrium conditions. Figure 10 displays temperature-dependent impedance spectra at various O_2 partial pressures (1%, 10%, and 100% O_2 corresponding to 10, 100, and 1000 mbar of O_2 in a He/O_2 mixture; total pressure 1000 mbar) at 1 Hz and a stimulation voltage of 20 mV. The samples were heated in the respective He/O_2 atmospheres to 773 K and subsequently cooled. At 773 K, an oxygen partial pressure-dependent concentration of vacancies is present and remains upon cooling, that is, three almost parallel cooling traces are obtained. The Arrhenius plots highlighted in Figure 10 reveal two temperature regimes for processes with different activation energies for all three oxygen partial pressure curves: one process with ~52 kJ mol^{-1} (measured between 343 and 373 K) and a second with around 90 kJ mol^{-1} (measured between 673 and 773 K). The process at lower temperatures with lower activation energy is only associated with the thermal activation of the charge carriers, i.e. electrons, since up to about 673 K no reversible oxygen vacancy formation in oxygen is observed (constant vacancy concentration). At higher temperatures ($T \geq$ 723 K), oxygen partial pressure dependent, reversible formation of vacancies sets in. The activation energy at these temperatures thus exhibits combined contributions both from the thermal excitation of charge carriers and the thermal reaction equilibrium of the O^{2-} lattice ions with the O_2 gas atmosphere. The reversibility of oxygen vacancy formation at different oxygen partial pressures as a function of time at 773 K is highlighted in Figure 11, which emphasizes the reversible switching between different amounts of vacancies. Note that the step between 100% and 50% O_2 amounts to about 3 min and the hysteresis between 5% and 50% O_2 to about 10 min.

The question of how the impedance/conductivity is connected with the concentrations of oxygen vacancies is addressed in

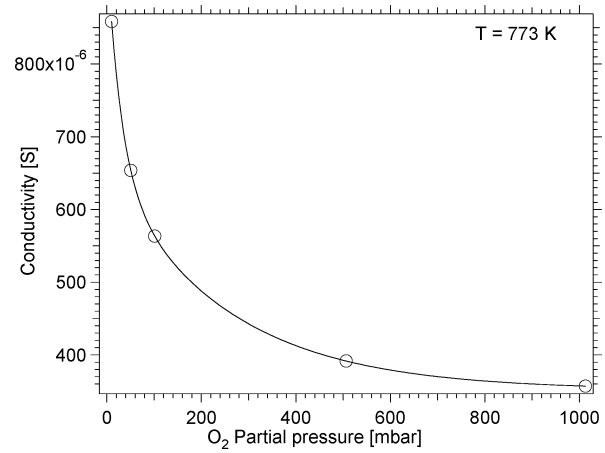

Figure 12. Conductivity as a function of the O_2 partial pressure (100%, 50%, 10%, 5%, and 1%, corresponding to 1000, 500, 100, 50, and 10 mbar of O_2 in a O_2/He mixture; total pressure 1000 mbar) at 773 K to reveal the dependence of the charge carrier concentration on the oxygen partial pressure.

Figure 12. The conductivity values correspond to averaged values of the plateaus of Figure 11 (after conversion of impedance into conductivity). The dependence of the conductivity on the oxygen partial pressure can be estimated on the pretext of the following assumptions ([*S*] or [1/Ω] as the unit of the electric conductivity in Siemens): (i) the number of excited charge carriers is proportional to the conductivity measured in [1/Ω] = [*S*], (ii) thermal excitation of charge carriers without the formation of oxygen vacancies is possible, corresponding to the limit of $p(O_2)$ at $p(O_2) \rightarrow \infty$, and (iii) the equilibrium of charge carrier formation/quenching is approximated by $2O^{2-} \leftrightarrow O_2 + 4e^- + 2\#$. Further assuming that the two electrons occupy one vacancy and both are delocalized in the conduction band, we arrive at the following equation for the equilibrium constant *K*:

$$K = p(O_2)\frac{[e^-]^4}{[O^{2-}]^2}$$

Assuming $[O^{2-}]$ is a constant in the bulk, the equation transforms into

$$K' = p(O_2)[e^-]^4 \quad \text{or} \quad [e^-] = \sqrt[4]{\frac{K'}{p(O_2)}}$$

The concentration of charge carriers $[e^-]$ is thus proportional to $p(O_2)^{-1/4}$, which apparently is very well supported by the experimental data.

4. Conclusions

We could unambiguously show that reduction of bcc In_2O_3 proceeds through a series of discernible reduction steps, which could be phenomenologically demonstrated by a combination of several techniques (TPR, TPD, impedance spectroscopy, XRD, and Raman spectroscopy). The major difficulty arises upon attempting to assign these reduction states to specific oxidation states or even well-ordered crystallographic phases associated with In redox states between +3 and 0. Two extreme cases can be pinned down safely: Below $T < 500$ K surface-limited reduction without detectable structural changes occurs, whereas at $T \geq 573$ K deep reduction toward In metal is observed. Open questions concern the structural consequences of progressive formation of In_2O_{3-x} species. Obviously, *x* has

to exceed a certain value to induce structural changes, such as those observed in Raman after reduction at $T \geq 523$ K. Whether these Raman features are related to heavily distorted building blocks of the original bcc In_2O_3 lattice or already represent building blocks of potential suboxidic phases cannot be decided on the basis of the present experiments.

As the motivation of the work was to some extent fuelled by previous work on β-Ga_2O_3, the present results should also be viewed in direct comparison with the results on β-Ga_2O_3, as outlined in detail in ref 10. Apparently, most of the differences between both oxides in terms of hydrogen surface chemisorption, desorption, and reactivity are related to the easier surface and bulk reduction of In_2O_3 and the subsequent formation of metallic In during reduction. Exposure of In_2O_3 to hydrogen occurs already at 300 K and up to ~400 K results in surface reduction, bonding of hydrogen, and formation of oxygen vacancies. Further increase of the reduction temperature yields reduction of surface-near regions and finally, above 500 K, bulk reduction occurs. At these temperatures, Raman spectra of reduced In_2O_3 samples suggest structural reordering. However, in contrast to similar experiments on β-Ga_2O_3, where the formation of surface OH groups, and, at higher temperatures, more strongly bound covalent Ga−H species were detectable by FT-IR, the transition between different chemisorbed H-containing species as a function of reduction temperature and thus, on clean or defective In_2O_3, could not be directly followed by spectroscopic techniques. Since there is very strong experimental evidence that hydrogen is indeed chemisorbed in a spectroscopically "invisible" way, we tentatively interpret this behavior as hydrogen bound to oxygen defects, but without the distinct formation of related directional (covalent) In−H bonds. Similarities to β-Ga_2O_3 include the easy quenching of oxygen vacancies by water, a process of paramount importance for reforming reactions.

Acknowledgment. The authors thank the FWF (Austrian Science Foundation) for financial support under project P20892-N19.

References and Notes

(1) Kominami, H.; Nakamura, T.; Sowa, K.; Nakanishi, Y.; Hatanaka, T.; Shimaoka, G. Low voltage cathodoluminescent properties of phosphors coated with In_2O_3 by sol-gel method. *Appl. Surf. Sci.* **1997**, *113−114*, 519–522.

(2) Ivanovskaya, M.; Gurlo, A.; Bogdanov, P. Mechanism of O_3 and NO_2 detection and selectivity of In_2O_3 sensors. *Sens. Actuators, B* **2001**, *77*, 264–267.

(3) Sanders, D.; Simon, U. High-throughput gas sensing screening of surface-doped In_2O_3. *J. Comb. Chem.* **2007**, *9*, 53–61.

(4) Umegaki, T.; Kuratani, K.; Yamada, Y.; Ueda, A.; Kuriyama, N.; Kobayashi, T.; Xu, Q. Hydrogen production via steam reforming of ethyl alcohol over nano-structured indium oxide catalysts. *J. Power Sources* **2008**, *179*, 566–570.

(5) Lorenz, H.; Stöger-Pollach, M.; Schwarz, S.; Pfaller, K.; Klötzer, B.; Penner, S. Novel methanol steam reforming activity and selectivity of pure In_2O_3. *Appl. Catal., A* **2008**, *347*, 34–42.

(6) Gervasini, A.; Perdigon-Melon, J. A.; Guimon, C.; Auroux, A. An in-depth study of supported In_2O_3 oxide as a potential environmental catalyst: The influence of the oxide support. *J. Phys. Chem. B* **2006**, *110*, 240–249.

(7) Zhang, D. H.; Li, C.; Han, S.; Liu, X. L.; Tang, T.; Jin, W.; Zhou, C. W. Electronic transport studies of single-crystalline In_2O_3 nanowires. *Appl. Phys. Lett.* **2003**, *82*, 112–114.

(8) (a) Otsuka, K.; Yasui, T.; Morikawa, A. The decomposition of water on the CO- or H_2-reduced indium oxide. *Bull. Chem. Soc. Jpn.* **1982**, *55*, 1768–1771. (b) Otsuka, K.; Takizawa, Y.; Shibuya, S.; Morikawa, A. Hydrogen production from water by In_2O_3 and K_2CO_3 using graphite, active carbon and biomass as reductants. *Chem. Lett.* **1981**, *3*, 347–350.

(9) Brinzari, V.; Korotchenkov, G.; Ivanov, M.; Nehasil, V.; Matolin, V.; Masek, K.; Kamei, M. Valence band and band gap photoemission study of (111) In_2O_3 epitaxial films under interactions with oxygen, water and carbon monoxide. *Surf. Sci.* **2007**, *601*, 5585–5594.

(10) Jochum, W.; Penner, S.; Föttinger, K.; Kramer, R.; Rupprechter, G.; Klötzer, B. Hydrogen on polycrystalline β-Ga_2O_3: surface chemisorption, defect formation and reactivity. *J. Catal.* **2008**, *256*, 268–277.

(11) Watson, W. W.; Shambon, A. The spectrum of indium oxide. *Phys. Rev.* **1936**, *50*, 607–609.

(12) Klemm, W.; Vogel, H. U. V. Messungen an Gallium-und Indium-verbindungen X. Über die Chalkogenide von Gallium und Indium. *Z. Anorg. Chem.* **1934**, *219*, 45–64.

(13) Klinedienst, K. A.; Stevenson, D. A. The determination of the standard gibbs energies of formation of indium oxides from e.m.f. measurements using a solid oxide electrolyte technique. *J. Chem. Thermodyn.* **1973**, *5*, 21–29.

(14) Anderson, T. J.; Donaghey, L. F. Solid-state electrochemical study of the standard Gibbs energy of formation of indium sesquioxide. *J. Chem. Thermodyn.* **1977**, *9*, 617–628.

(15) Brewer, L. Thermodynamic Properties of the Oxides and their Vaporization Processes. *Chem. Rev.* **1953**, *52*, 1–75.

(16) Van Dillen, A. J.; Geus, J. W.; de Wit, J. H. W. On the existence of In_2O. *J. Chem. Thermodyn.* **1978**, *10*, 895–896.

(17) Broch, N. C.; Christensen, A. N. On the Existence of Crystalline In_2O. *Acta Chem. Scand.* **1966**, *20*, 1996–1997.

(18) Yin, W.; Su, J.; Cao, M.; Ni, C.; Cloutier, S. G.; Huang, Z.; Ma, X.; Ren, L.; Hu, C.; Wei, B. $In(OH)_3$ and In_2O_3 Micro/Nanostructures: Controllable NaOAc-Assisted Microemulsion Synthesis and Raman Properties. *J. Phys. Chem C* **2009**, *113*, 19493–19499.

(19) Kaur, M.; Jain, N.; Sharma, K.; Bhattacharya, S.; Roy, M.; Tyagi, A. K.; Gupta, S. K.; Yakhmi, J. V. Room-temperature H_2S gas sensing at ppb level by single crystal In_2O_3 whiskers. *Sens. Actuators, B* **2008**, *133*, 456–461.

(20) Baszczuk, A.; Jasiorski, M.; Nyk, M.; Hanuza, J.; Maczka, M.; Strek, W. Luminescence properties of europium activated $SrIn_2O_4$. *J. Alloys Compd.* **2005**, *394*, 88–92.

JP1017423